Electrochimica Acta 579 (2026) 149982

Contents lists available at ScienceDirect

Electrochimica Acta

journal homepage: www.journals.elsevier.com/electrochimica-acta

Degradation of bifunctional α-MnO_2/NiO@Ni gas-diffusion electrodes for Zn-air batteries: Space-resolved Ni chemical-state evolution mapped by soft X-ray spectral ptychography

Alessandro Alleva [a,*], Francesco Guzzi [b], Massimo Frittelli [c], George Kourousias [b], Valentina Bonanni [b], Alessandra Gianoncelli [b], Ivonne Sgura [c], Milan Žižić [b], Benedetto Bozzini [a]

[a] Department of Energy, Politecnico di Milano, via Lambruschini 4, Milano, 20156, Italy
[b] Elettra - Sincrotrone Trieste S.C.p.A. S.S, 14, km 163.5 in Area Science Park, Trieste-Basovizza, 34149, Italy
[c] Università del Salento, Dipartimento di Matematica e Fisica "E. De Giorgi", via per Arnesano, Lecce, 73100, Italy

ARTICLE INFO

Keywords:
Ptychography
Gas diffusion electrode
Zinc-air battery
Impedance spectroscopy
Degradation

ABSTRACT

The degradation of Mn-based gas diffusion electrodes (GDEs) limits the durability of rechargeable Zn–air batteries. In our previous study [1], scanning transmission X-ray microscopy (STXM) at the Mn L-edge revealed pathways of Mn reduction and dissolution, but could not resolve Ni, whose nanometric dispersion and weak absorption made it undetectable. Here, we apply soft X-ray ptychography at the Ni L-edge to the same electrodes. The higher spatial resolution of ptychography allowed detection of Ni distributions that were inaccessible by STXM, while Kramers–Kronig (KK) reconstruction of phase spectra provided absorption-equivalent information in regions where the magnitude signal was unusable. The workflow was validated by direct comparison of KK-converted and magnitude spectra, and by reconstructing hybrid datasets combining both channels. Applied to three bifunctional samples, this approach revealed distinct Ni–Mn correlations: localized oxidized Ni overlapping with Mn(II) in the low-Ni sample, more homogeneous Ni distribution stabilizing Mn redox activity at higher Ni loading, and unexpected Ni–Mn(II) co-localization under zincate cycling, consistent with dissolution–reprecipitation processes. These results demonstrate that ptychography, combined with KK-based spectral reconstruction, extends nanoscale spectromicroscopy beyond the limits of absorption contrast and provides new insights into the cooperative behavior of Ni and Mn in bifunctional electrocatalysts. The spectromicroscopy findings are accompanied by the detailed electrochemical analysis of GCD ageing followed by chronopotentiometric and electrochemical impedance measurements, which consistently identify the optimized Ni loading as the most stable electrode architecture.

1. Introduction

The performance and durability of bifunctional catalysts remain among the most critical challenges for the practical implementation of rechargeable zinc–air batteries (ZABs) [2–5]. Among candidate materials, manganese oxides have attracted particular attention for the oxygen reduction (ORR) and oxygen evolution reactions (OER) due to their earth abundance, structural versatility, and tunable redox chemistry [6–11]. Despite these advantages, Mn-based catalysts often suffer from instability under electrochemical cycling, as structural rearrangements, dissolution, and disproportionation reactions progressively reduce the number of active sites and limit long-term performance [8,11]. To address these limitations, strategies involving the incorporation of Ni/NiO have been pursued, as nickel species not only provide additional redox buffering capacity but also improve conductivity and stabilize Mn oxidation states [1,12,13]. Nevertheless, the nanoscale mechanisms underlying the cooperative behavior of Ni and Mn, as well as the specific degradation pathways at the level of individual catalyst domains, remain insufficiently understood. Soft X-ray spectromicroscopy has proven invaluable for exploring battery materials and their degradation by enabling spatially resolved mapping of chemical states [1,14–17]. In our previous work [1], scanning transmission X-ray microscopy (STXM)

* Corresponding author.
E-mail address: alessandro.alleva@polimi.it (A. Alleva).

https://doi.org/10.1016/j.electacta.2026.149982
Received 26 June 2026; Received in revised form 8 September 2026; Accepted 11 September 2026
Available online 12 September 2026
0013-4686/© 2026 The Authors. Published by Elsevier Ltd. This is an open access article under the CC BY license (http://creativecommons.org/licenses/by/4.0/).

was used to identify the evolution of Mn valence states within α-MnO_2-based gas diffusion electrodes (GDEs). That study revealed correlations between Ni content, electrode architecture, and the onset of Mn reduction and dissolution. However, STXM is intrinsically limited by its spatial resolution, defined by the X-ray optics used, and its reliance on absorption contrast, which becomes problematic when studying ultrathin or low absorbance systems. In such cases, the absorption signal is often too weak to yield reliable spectra, restricting insights precisely at the scale where degradation processes may initiate. Integrating Differential Phase Contrast (DPC) maps is definitely possible, but harder to achieve and possibly leading to noisier and lower resolution information [18,19]. Soft X-ray ptychography offers a promising solution to these limitations. Based on coherent diffraction imaging and iterative phase retrieval, ptychography achieves spatial resolutions down to ~10 nm while simultaneously delivering both amplitude and phase contrast [20–22]. The phase channel is particularly advantageous for thin or weakly absorbing samples, as phase shifts remain detectable in regimes where absorption is negligible [23,24]. This makes ptychography uniquely suited for probing electrocatalyst nanostructures, bridging the gap between structural and spectroscopic analysis. Recent methodological advances further enhance its relevance: absorption-like spectra can be reconstructed from phase data using the Kramers–Kronig (KK) relation, enabling chemically interpretable mapping even where direct absorption is inaccessible [25,26].

In this work, we carried out galvanostatic charge-discharge (GCD) ageing of different electrode configurations, monitored the evolution of their electrochemical state by chronopotentiometry and galvanostatic electrochemical impedance spectroscopy and performed hyperspectral microscopy characterization of the Ni electrocatalyst. This extends our previous study [1] by directly building on the Mn chemical-state maps reported there, which provided spatially resolved insights of α-MnO_2 degradation pathways in GDEs. While those results identified critical mechanisms of Mn catalyst degradation, the role of nickel in mitigating these effects and enhancing device durability remained largely unresolved, as its nanometric dispersion rendered it effectively undetectable in absorption-based STXM. By applying KK-based spectral reconstruction to soft X-ray ptychography at the Ni L-edge, developing on the approach pioneered in [27], we overcome this limitation and reveal the local spectroscopic signature of Ni within the same systems. In particular, we validate the method by comparing KK-derived phase spectra with conventional absorption data where available, and then use the reconstructed Ni maps to establish correlations with the previously identified Mn redox environments. In doing so, we not only extend the interpretive framework of our earlier work but also demonstrate how ptychography uniquely enables the detection and analysis of nanoscale, weakly absorbing species such as dispersed Ni species. Importantly, whereas our previous study provided spatially resolved information only on Mn redox evolution, the present approach enables the Ni chemical state to be mapped within the same electrode fragments and directly compared with the previously determined Mn distributions. This provides previously inaccessible information on the local Ni–Mn relationships associated with the different degradation behaviors of the investigated electrodes. This capability provides access to degradation phenomena that were previously inaccessible, opening new opportunities for mechanistic insight into the cooperative behavior of Ni and Mn as bifunctional electrocatalysts.

2. Materials and Methods

2.1. Fabrication of gas diffusion electrodes

The Ni–MnO_2 gas diffusion electrodes (GDEs) investigated in this work were prepared following the procedure reported in [1,13]. In brief, α-MnO_2 nanorods were synthesized via a solution-based route and subsequently mixed with Ni/NiO nanoparticles (APS 5–20 nm, 99.9% (metals basis), Alfa Aesar), Carbon Black (CB, Csingle bondNERGY SUPER C65, Imerys Graphite & Carbon), and PTFE binder (59 wt%, 3M™ Dyneon™ PTFE TF 5060GZ) to form the catalyst ink. The suspension was deposited onto carbon paper substrates (Toray Paper 090-TGP-H-090 60 wt%) by spray coating, targeting a catalyst loading of approximately 5 mg cm^{-2}. The resulting electrodes were dried and thermally treated following the same conditions previously reported for this GDE preparation procedure [1,13].

2.2. Electrochemical cycling

Electrochemical ageing was carried out in a three-electrode cell (Gaskatel GmbH, Flex cell) using 6 M KOH electrolyte, with a Pt wire counter electrode (AMEL s.r.l.) and a Hg/HgO reference electrode. The 6 M KOH concentration was selected to provide the highly conductive alkaline environment conventionally employed for Zn–air battery operation and, importantly, to maintain direct comparability with our previous ageing studies on the same GDE system [1,13]. Ageing was performed by means of a galvanostatic charge-discharge (GCD) protocol consisting of alternating ORR and OER galvanostatic steps. The cathodic current density was kept constant throughout the experiment, whereas the anodic current density was progressively increased in successive cycles in order to evaluate the effect of increasingly demanding OER conditions on electrode degradation. This approach allowed the ORR response not only to provide a metric of the cathodic performance, but also to probe the degradation induced by the preceding OER steps. Galvanostatic electrochemical impedance spectra were acquired at the end of each cathodic step, enabling dynamic electrochemical monitoring of the evolution of the electrode state throughout the GCD ageing protocol. GCD tests were carried out in 6 M KOH, either in the absence of zincates (samples B1 and B2) or with the addition of 0.1 M ZnO (sample B3), consistently with the conditions adopted in our previous study [1].

2.3. Preparation of the samples for ptychography at the Ni L-edge

To prepare the samples for spectromicroscopy, the active material was scraped off from the cycled GDEs and suspended in isopropanol at a concentration of 2 mg mL^{-1}. The suspension was sonicated for 1 min using a tip sonicator (UP200 St, Ultrasonic processor, Hielscher Ultrasonics GmbH) to promote homogeneous dispersion of the catalyst fragments. A small volume of the resulting solution was then drop-cast with a micropipette onto gold TEM grids covered with a formvar support film (Agar Scientific, Square Pattern 100 Mesh TEM Support Grids). This preparation route was chosen to obtain well-dispersed particles while minimizing the formation of thick bundles of nanowires, which would hinder X-ray transmission. To verify the quality and distribution of the deposited material, the grids were first mapped by SEM prior to spectromicroscopy. The resulting grids were subsequently used as the common platform for both the STXM analyses reported in [1] at the Mn L-edge and the present ptychography measurements at the Ni L-edge.

2.4. Data acquisition and ptychography reconstructions

Data acquisition was conducted at the TwinMic spectro-microscopy beamline [28,29], exploiting a typical configuration for Coherent Diffraction Imaging (CDI) experiments [28]; a Fresnel gold zone plate (600 μm diameter, 50 nm outermost zone width) was placed 250 μm upstream out-of-focus to generate a 6 μm illumination probe on the sample, thereby introducing phase curvature to the illumination. Diffraction patterns were recorded in transmission geometry using a direct-detection 4 M pixel sCMOS camera (AXIS-SXRF-v2, 11 μm pixel size) positioned 70 cm downstream of the sample, with an exposure time of 0.1 s. Stacks of ptychography scans were acquired across the Ni L-edges in the 834–874 eV energy range. Energy calibration was performed by using a 50 nm Ni layer, deposited on a Si_3N_4 window, as a reference standard. In order to optimise both the energy resolution in the ranges that are crucial for chemical-state evaluation, and the overall

experiment time, a step of 1 eV was chosen in the pre-edge range from 834 to 841 eV and in the post-edge zone from 867 to 874 eV. On the other hand, the range around the first edge from 841 to 853 eV and from 861 to 867 eV was scanned with a higher resolution step of 0.25 eV, while in the less diagnostic range of 853 to 861 eV, the energy step was set to 0.5 eV. During the XANES acquisition sequence, the sample-to-focus distance was adjusted to keep consistent illumination conditions across the energy scan. Each ptychography dataset consisted of 13 × 13 diffraction patterns, acquired by scanning the sample in a regular grid with a step size of 2 μm. Ptychographic reconstructions were performed post-acquisition using the SciComPty software framework [30], implementing the multi-mode Regularized Ptychographic Iterative Engine (M-RPIE) algorithm [30,31]. This approach jointly reconstructs the complex object transmission function and the partially coherent illumination, modeled as an incoherent sum of 3–5 orthogonal modes, that are initialized with a spherical wave with the same defocus corrupted by Gaussian noise. Probe orthogonalization was applied every 10 iterations to suppress noise and minimize artefact formation. Sample position errors and uncertainties in photon energy were corrected using an Adam-based position refinement routine [30,32]. The reconstruction was iterated for 1000 steps. The alpha and beta parameters for the RPIE algorithm were set respectively to 0.5 for the object and 0.25 for the probe. Reconstructions were performed independently for each energy, in sequence. However, to promote consistency between adjacent energies and accelerate convergence, the illumination model was initialized with the final probe obtained from the previous energy step. The resulting stack of complex-valued object reconstructions was resampled to a common reference grid (smallest pixel-size of 43 nm) and aligned using phase-correlation techniques. The aligned dataset served as input for subsequent conventional XANES analysis [33].

2.5. XANES data analysis workflow

The ptychography datasets consisted of energy-resolved complex reconstructions, from which both magnitude and phase stacks were available. The analysis was structured in the following steps:

i. A reference spectrum was extracted from a manually selected, non-background region of the stack.
ii. Each pixel spectrum was compared with the reference using the cosine similarity metric. This criterion was chosen for its sensitivity to spectral shape rather than absolute intensity or small energy shifts. For the magnitude channel, the similarity threshold was selected empirically by inspecting the transition between spectra retaining the characteristic Ni L-edge shape and spectra increasingly dominated by noise. Spectra immediately above and below the selected threshold were visually inspected to verify that the cutoff corresponded to the loss of chemically interpretable spectral features. The threshold was therefore used as a spectral-quality criterion rather than as a physically meaningful parameter. Spectra immediately above and below the selected threshold were visually inspected to verify that the cutoff corresponded to the loss of chemically interpretable spectral features.
iii. Based on a similarity threshold, pixels were classified as containing either a “good” magnitude spectrum, a “good” phase spectrum, both, or neither.
iv. In regions where both spectra were considered reliable, the phase data were transformed into absorption spectra using the KK relation [26]. This step was used only initially and for validation purposes, by comparing the KK-converted spectra with the corresponding magnitude spectra. For quantitative validation, the position of the main Ni L_3 feature was compared pixel-by-pixel between magnitude and KK-converted phase spectra in regions where both channels passed the reliability criterion; prior to peak localization, both spectra were subjected to the same Savitzky-Golay smoothing procedure.
v. A complete hybrid stack was reconstructed using the classification maps. Pixels with good magnitude spectra retained their original values, pixels with good phase-only spectra were reconstructed through the KK transform, and background pixels were set to zero.

From the reconstructed dataset, the chemical-state composition, expressed as Ni(0)/Ni(II), was estimated with the method proposed in [32]. Briefly, the energy position of the measured XAS peak was associated with the chemical-state ratio through the linear combination of peak positions for the pure chemical forms. These maps were then correlated with the Mn redox-state distributions previously obtained from the same TEM grids at the Mn L-edge [1]. Details of the implementation, including the KK algorithm and the Python functions used for classification and reconstruction, are reported in the Supporting Information.

2.6. Electrochemical impedance spectrometry

Electrochemical impedance spectra were analysed using an equivalent-circuit approach aimed at extracting global resistive descriptors of cycling, refraining from attempting a phenomenological assignment of all physical processes occurring in the porous GDE. A two-time-constant model, R_s–(R_1||CPE_1)–(R_2||CPE_2), was used as the main comparative framework. The series resistance R_s and the polarization resistance $R_{pol} = R_1 + R_2$ were retained as the primary descriptors. Individual contributions R_1 and R_2 were interpreted only when the two processes were sufficiently resolved according to the diagnostic criteria reported in the Supporting Information. Details of the fitting workflow, diagnostic classification criteria, representative fitting examples and the complete evolution of the fitted parameters are reported in the Supporting Information.

3. Results

3.1. Background on samples and previous findings

The present work builds directly on our previous study [1], where the degradation behavior of gas diffusion electrodes, prepared either as monofunctional α-MnO_2 systems or as bifunctional catalysts incorporating Ni/NiO nanoparticles, was analyzed by STXM at the Mn L-edge. That investigation identified distinct pathways of Mn reduction and dissolution, and highlighted correlations between Mn redox states, Ni content, and ageing protocols. In this work, three bifunctional samples were considered. They differed in Ni loading and in the presence or absence of zincates during electrochemical cycling. The main observations from [1], together with the sample characteristics and the current work findings, are summarized in Table 1. In particular, the STXM results revealed that the lowest Ni content (B1) correlated with pronounced Mn reduction, whereas optimized Ni loading (B2) [13] promoted more stable Mn redox cycling. In the presence of zincates (B3), the same Ni content no longer prevented degradation, suggesting that zincate-induced Mn(II) formation processes dominate under these conditions. These findings provide the framework for the present study. Here, the same samples (B1-B3) are re-examined at the Ni L-edge using ptychographic spectromicroscopy. The aim is to complement the previously obtained Mn chemical maps with Ni-specific information, thereby enabling a correlative picture of Ni–Mn interactions during degradation.

3.2. Electrochemical performance and impedance evolution during ageing

Fig. 1 summarizes the evolution of the average electrode potential during the GCD ageing protocol. The average electrode potential and its standard deviation are reported for each galvanostatic step and for all three investigated samples. The three electrodes exhibited markedly

Table 1
Overview of the samples investigated in [1] and re-examined in the present work.

Sample	Ni content (wt%)	Ageing conditions	Main Mn-related findings from [1]	Mean ± sdev Ni(0)/Ni(II)	Total number of pixel used in the analysis
B1	10	OER/ORR cycling without zincates	Localized Mn (II) accumulation, insufficient stabilization by Ni	0.589 ± 0.27	749
B2	23	OER/ORR cycling without zincates	More homogeneous Mn distribution, balanced Mn (III)/Mn(IV) ratios	0.624 ± 0.23	9714
B3	23	OER/ORR cycling with zincates	Enhanced Mn (II) accumulation, evidence of dissolution/ redeposition	0.605 ± 0.28	17,970

different behaviours. B1 showed the strongest performance decay, with progressively increasing OER potentials and progressively decreasing ORR potentials. B2 remained comparatively stable throughout the ageing procedure, whereas B3 displayed an intermediate behaviour. The ranking derived from the electrochemical performance (B2 > B3 > B1) indicates that the optimized Ni loading markedly improves electrode stability under zincate-free conditions, whereas the presence of zincates partially suppresses this beneficial effect. The relatively limited standard deviations compared with the overall variation of the average potential indicate that the observed trends mainly originate from progressive electrode degradation rather than from short-term fluctuations during individual ageing steps.

To further investigate the origin of these performance differences, electrochemical impedance spectroscopy measurements acquired at selected stages of the GCD ageing protocol were analysed. The corresponding evolution of the impedance-derived polarization resistance is summarized in Fig. 2. Since the equivalent circuit was not intended to provide a unique physical deconvolution of the porous GDE response, the discussion focuses on the polarization resistance, $R_{pol} = R_1 + R_2$, as described in Section 2.6. The impedance analysis closely paralleled the electrochemical performance observed during GCD ageing (Figs. 1 and 2). Sample B1 exhibited the largest increase in polarization resistance, with R_{pol} increasing from 0.582 Ω to 4.25 Ω (+631%), confirming the severe degradation already evident from the galvanostatic response. Throughout ageing, the impedance spectra remained predominantly classified as resolved (Figure S3), indicating that the two relaxation processes remained sufficiently separated to allow reliable extraction of R_{pol}. Consequently, the increase in polarization resistance reflects a genuine deterioration of the electrode electrochemical response rather than a loss of parameter identifiability. In contrast, B2 showed only a limited increase in polarization resistance, from 0.555 Ω to 0.645 Ω (+16%) (Fig. 2), consistently with its stable galvanostatic behaviour (Fig. 1). The impedance response remained remarkably stable throughout the ageing protocol, indicating that the electrochemical processes governing the electrode response were only minimally affected by repeated cycling. Sample B3 displayed an intermediate evolution, with R_{pol} increasing from 1.08 Ω to 2.89 Ω (+169%) (Fig. 2). Degradation became more evident during the later stages of GCD ageing (Fig. 1), while the impedance spectra exhibited the highest incidence of borderline and collapsed classifications during the early stages of cycling (Figure S3). This behaviour indicates that the characteristic timescales of the dominant electrochemical processes progressively converged, making the individual impedance contributions increasingly difficult to distinguish, and is consistent with the onset of a more heterogeneous degradation mechanism under zincate-containing conditions, where multiple overlapping processes contribute simultaneously to the overall electrode response.

Overall, the electrochemical characterization reported in Figs. 1 and 2 identifies three distinct ageing behaviours: (i) rapid degradation for B1, (ii) limited degradation for B2 and (iii) intermediate degradation for B3, corresponding to increases in R_{pol} of 631%, 16% and 169%, respectively. As discussed in the following sections, this sample-to-sample ranking is consistent with the nanoscale chemical-state observations provided by the correlative Mn STXM and Ni L-edge ptychography analyses. This comparison is intended to establish consistency between independently obtained electrochemical and spectromicroscopic observations rather than a direct quantitative correlation among descriptors measured at different spatial scales.

3.3. *Validation of the data analysis workflow*

The reliability of the spectral reconstruction procedure was first

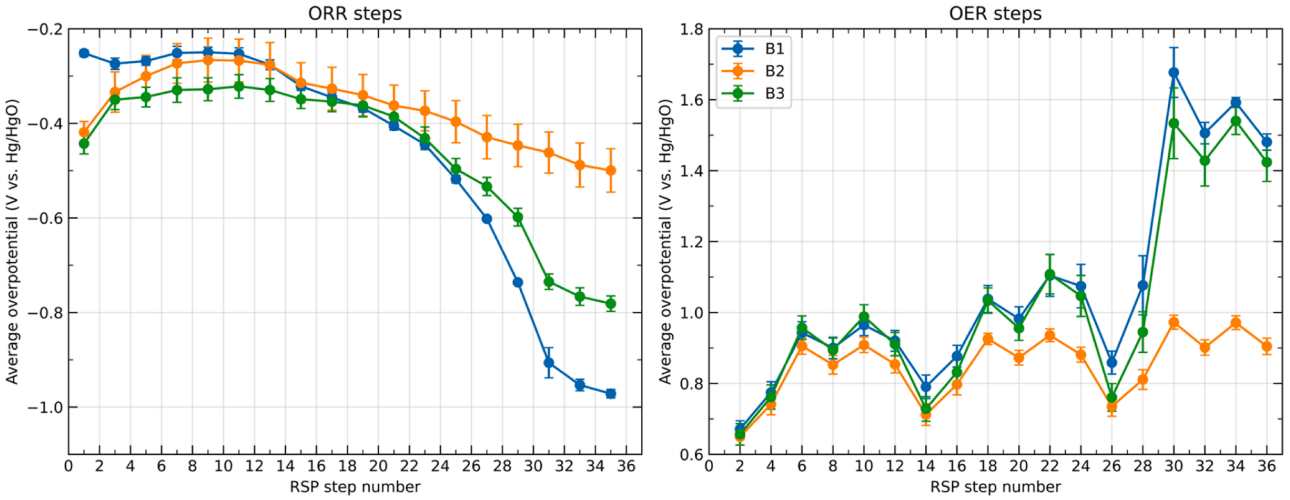


Fig. 1. Evolution of the average electrode overpotential during GCD ageing for samples B1, B2 and B3. Left: ORR steps. Right: OER steps. Error bars represent the standard deviation of the electrode potential during each ageing step.

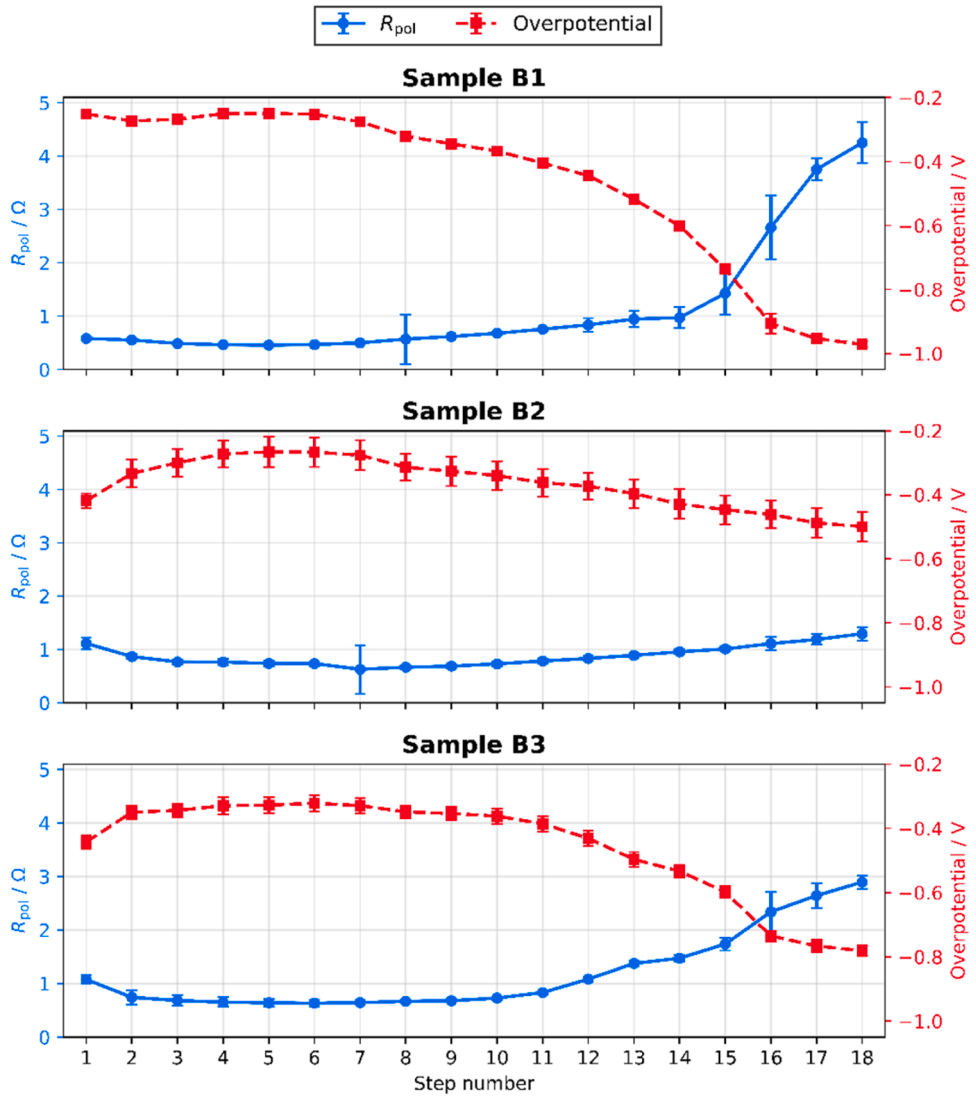


Fig. 2. Evolution of impedance-derived polarization resistance (R_{pol}) and electrode overpotential during ageing for samples B1, B2 and B3. Error bars represent the fitting confidence interval for R_{pol} and the standard deviation of the measured overpotential over the step duration.

evaluated on the Ni L-edge ptychography datasets. The analysis was carried out in three consecutive steps: classification of spectra by cosine similarity, validation of the KK transformation, and reconstruction of a complete hybrid stack.

3.3.1. *Classification of reliable spectra*

A reference spectrum was extracted from a non-background region of both the magnitude and phase stacks. Each pixel spectrum was then compared to this reference using the cosine similarity metric. Fig. 3 shows the result of this procedure for magnitude (panel a) and phase (panel b). In each case, the top image corresponds to the raw contrast, the middle overlay highlights the pixels that passed the similarity threshold, and the bottom trace shows the reference spectrum used. The classification of individual pixels was further refined by combining the magnitude and phase similarity maps. Four categories were defined: background (neither reliable), phase only, magnitude only, and both. Fig. 4a shows the resulting classification map, while Fig. 4b provides a zoom-in on a representative area. The average spectra corresponding to each class are reported in Figs. 4c (magnitude) and 4d (phase), confirming the consistency of the approach.

3.3.2. *Validation of the KK transformation*

In regions where both phase and magnitude spectra were found to be reliable, the KK transformation was applied to the averaged phase spectrum and the result compared with the corresponding averaged magnitude spectrum (Fig. 5a). The close match demonstrates that the KK relation can successfully reproduce absorption-like features when applied under consistent conditions. To complement the representative comparison shown in Fig. 5a, the agreement was also evaluated quantitatively on a pixel-by-pixel basis over the entire set of 1309 pixels for which both magnitude and phase spectra passed the reliability criterion. The median absolute error in the position of the main Ni L_3 spectral feature was 0.26 eV, with 64.2% and 77.0% of the evaluated pixels showing deviations within 0.5 and 0.75 eV, respectively. To test its applicability in less favorable cases, the transformation was also applied to a representative phase spectrum from a phase-only region. The resulting KK-converted spectrum (Fig. 5b) recovered well-defined spectral features that were not discernible in the corresponding magnitude spectrum, which was dominated by noise. This result demonstrates that the method can provide chemically interpretable information even in regions where absorption contrast alone is insufficient.

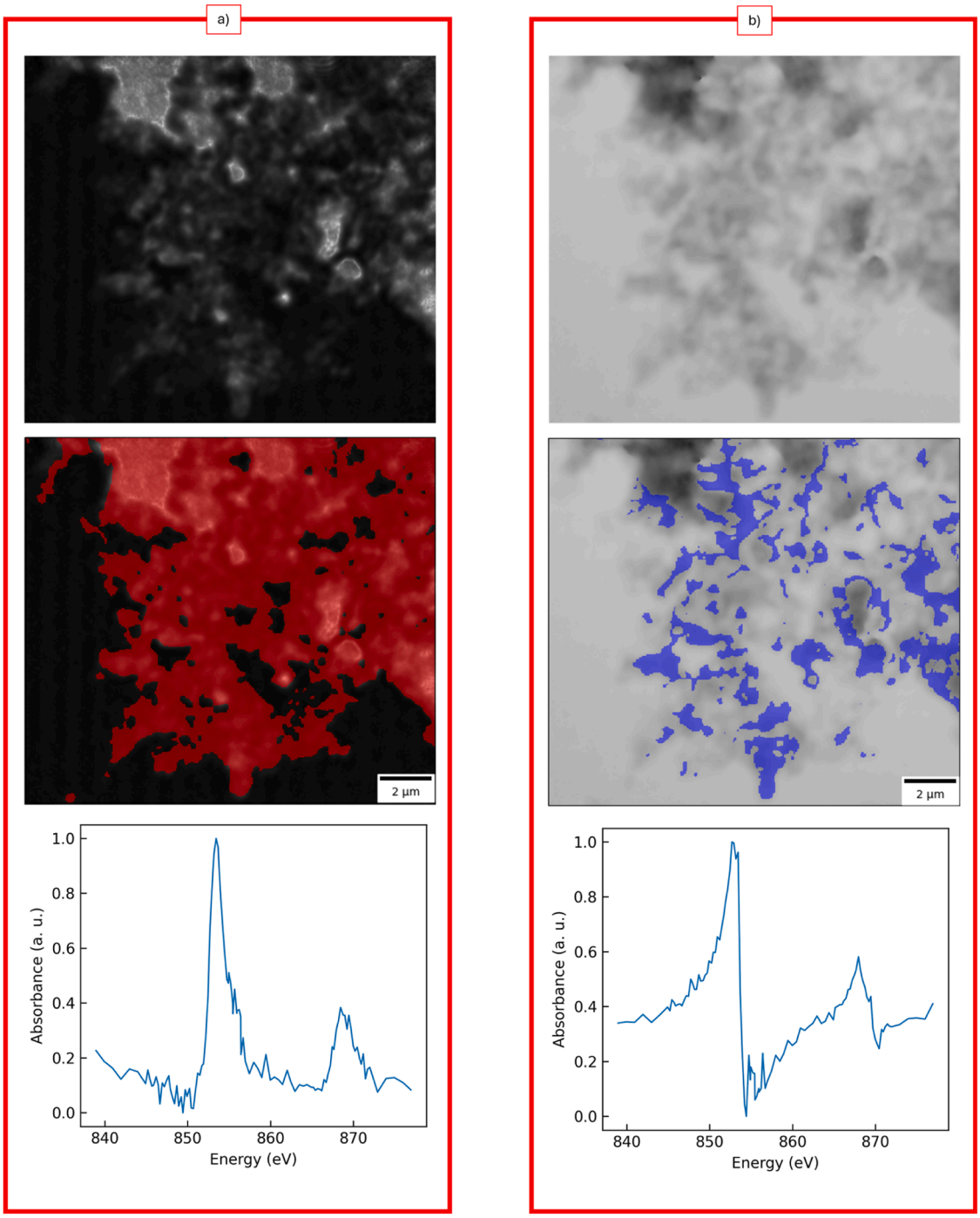


Fig. 3. Detection of representative pixels for spectral validation, example on sample B3. (a) Magnitude stack analysis. From top to bottom: grayscale contrast image, overlay showing the pixels selected as having spectra similar to the reference (based on cosine similarity), and the reference magnitude spectrum. (b) Phase stack analysis, shown analogously.

3.3.3. Reconstruction of a hybrid spectral stack

Based on the classification maps, a pixel-wise reconstruction of the complete absorption-equivalent dataset was carried out. Pixels classified as magnitude or both retained their original absorption values, while those classified as phase only were reconstructed from the corresponding phase spectra using the KK transform. Background pixels were excluded. This procedure enabled the generation of a complete dataset in which chemically interpretable absorption contrast was recovered even in regions where the original magnitude signal was weak or unavailable. Together, these results demonstrate that the workflow reliably identifies meaningful spectra, validates the KK transformation, and reconstructs hybrid datasets that extend the interpretability of ptychographic measurements beyond what is accessible from absorption contrast alone.

3.4. Results on ni–mn correlation in aged electrodes

3.4.1. Analytical rationale

The reconstructed ptychography datasets at the Ni L-edge provide access to the spectral evolution of nickel within the same electrode fragments previously analyzed at the Mn L-edge [1]. By mapping this parameter across the field of view and comparing it with the Mn redox

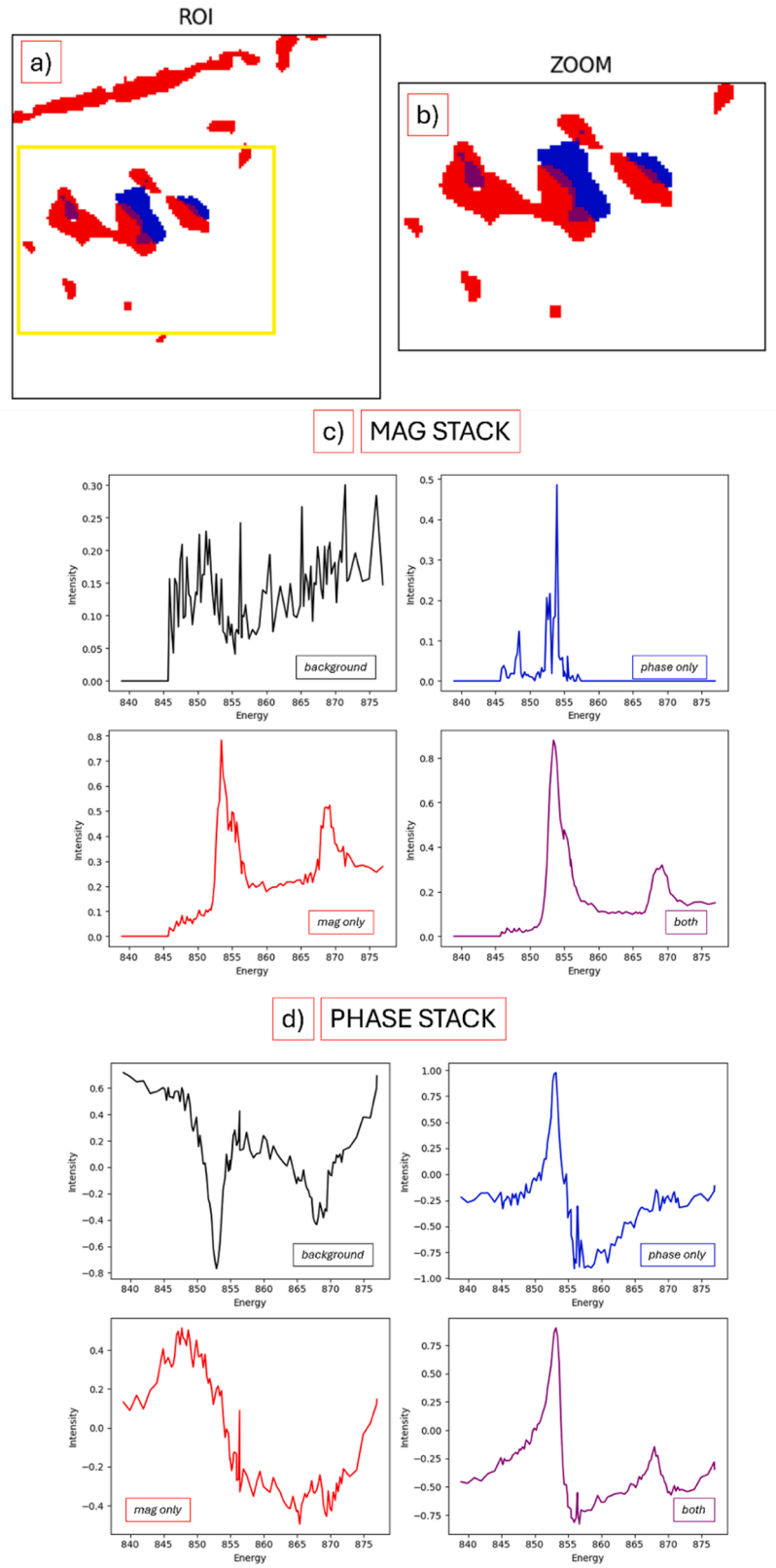


Fig. 4. Classification of pixels based on cosine similarity, example on sample B1. (a) Combined classification map showing four categories: background (white), phase only (blue), magnitude only (red), and both (purple). (b) Zoom-in of a representative region illustrating the spatial distribution of classes. (c) Average spectra from the magnitude stack for each category. (d) Average spectra from the phase stack for the same regions.

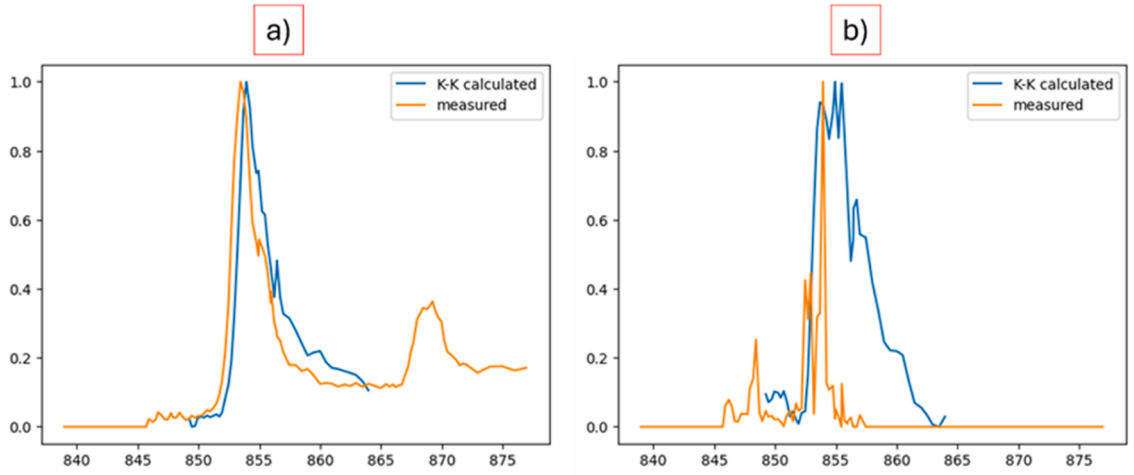


Fig. 5. Comparison of original and KK-converted spectra. (a) Overlay of the averaged magnitude spectrum and KK-converted phase spectrum from the purple region of Fig. 2. (b) Overlay of the KK-converted spectrum from a representative blue-region phase signal with the corresponding magnitude spectrum from the same location (Fig. 2). The KK transform was applied only within a limited energy range to reduce computation time and because this specific interval contains the spectral features of interest. The close match validates the reliability of the KK transformation for extracting absorption-like information from phase contrast data.

maps obtained in [1], correlations between Ni oxidation and Mn speciation could be established. In particular, zones characterized by high Mn(II)/Mn(IV) ratios are indicative of over-reduced and electrochemically inactive species, whereas regions where the Mn(III)/Mn(IV) ratio approaches unity reflect active and reversible redox cycling. Cross-analysis of the Ni L-edge maps with these Mn distributions allows identification of domains where nickel plays a stabilizing role versus areas where degradation processes dominate. This rationale provides the basis for the comparative analysis of the three bifunctional samples (B1-B3), which differ in Ni content and ageing conditions (Table 1). More generally, chemical-state maps describing the spatial distribution of electrochemically generated phases can be interpreted within the framework of morphochemical coupling between local electrode morphology and surface chemistry. This approach has been formalized through the DIB model [34,35], which provides a quantitative description of electrochemical phase formation and its spatial organization. Previous studies have shown that the model parameters can be identified from spatially resolved spectromicroscopy data using either conventional fitting procedures [36] or AI-based approaches [37]. In the present case, the applicability of this framework was assessed by fitting the two representative chemical-state maps reported in Fig. 6b. The successful fits provide a proof of feasibility for the quantitative interpretation of the present spectromicroscopy maps in terms of the physicochemical parameters of the morphochemical model. An exhaustive model-based analysis of all the acquired maps is beyond the scope of the present work; the mathematical formulation, fitting procedure and representative results are therefore reported in the Supporting Information. The spatial correlations discussed below refer to the specific electrode fragments investigated by correlative spectromicroscopy and should not be interpreted as a statistical representation of the entire GDE. Although each map contains a large number of spatially resolved pixels, these pixels do not constitute independent experimental replicates. Nevertheless, across the regions examined, no contradictory trends were observed and the characteristic spatial features associated with each sample were consistently encountered. These observations therefore suggest that the identified trends are reproducible within the investigated material, although establishing their statistical representativeness at the electrode scale would require systematic sampling of

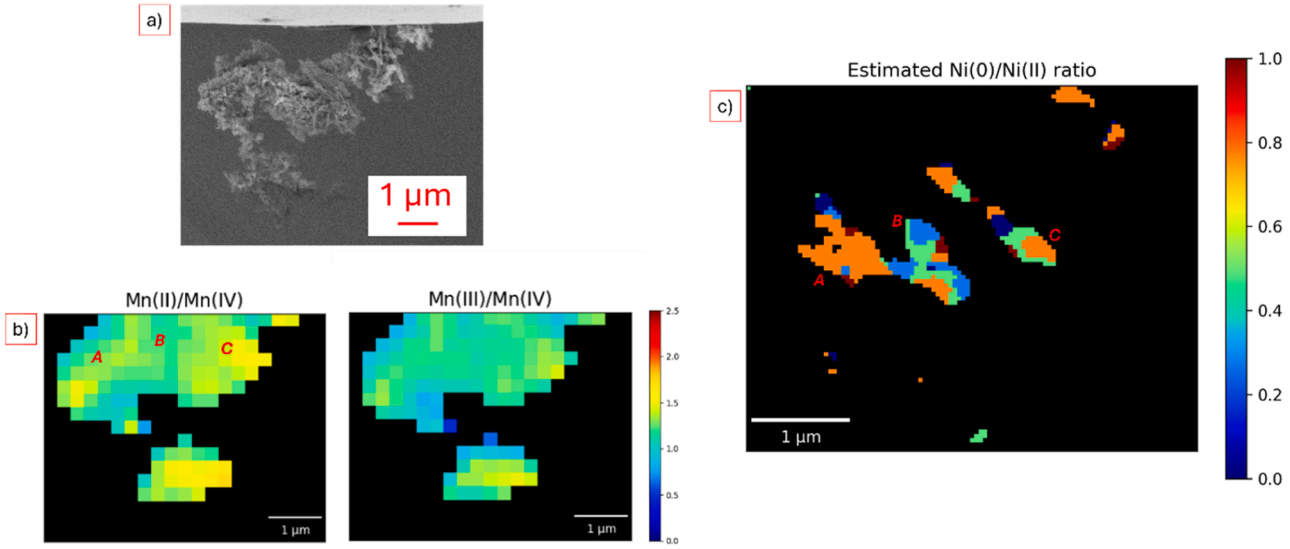


Fig. 6. Analyses on sample B1 (a) SEM image of the cluster under analysis. (b) Chemical ratio maps: Mn(II)/Mn(IV) (left) and Mn(III)/Mn(IV) (right). (c) Ni(0)/Ni(II) distribution map. Letters A, B, and C indicate matched points across all panels.

multiple independent regions and replicate electrodes, beyond the scope of the present work, the aim of which was to introduce the method and apply it to a close-knit group of GDE samples.

3.4.2. *Bifunctional GDE with low Ni/NiO content*

Sample B1 contained 10 wt% Ni and was aged under repeated OER/ORR cycling in the absence of zincates. In our previous work [1], the Mn speciation maps revealed extensive reduction of MnO_2, with large regions dominated by Mn(II) and only limited domains maintaining a balanced Mn(III)/Mn(IV) ratio. This behavior was attributed to insufficient stabilization of Mn by the low Ni content. The reconstructed Ni (0)/Ni(II) ratio map is shown in Fig. 6c, together with the Mn chemical-state maps (Fig. 6b). The Ni signal is highly localized, with isolated regions exhibiting low Ni(0)/Ni(II) ratios consistent with oxidized Ni. These areas overlap spatially with Mn domains enriched in Mn(II)/Mn(IV), indicating that Ni tends to accumulate in zones where Mn has already undergone irreversible reduction. In contrast, regions with higher Ni(0)/Ni(II) ratio correlate with areas where Mn(III)/Mn (IV) approaches unity, corresponding to zones that retain catalytic activity. The average Ni(0)/Ni(II) ratio for sample B1 was 0.589 ± 0.27 (Table 1). The significant spatial heterogeneity of the Ni oxidation state, combined with the extensive Mn reduction observed in [1], suggests that the low Ni loading in B1 does not provide effective redox buffering, leading to accelerated Mn degradation. This interpretation is consistent with the electrochemical performance observed during GCD ageing, reported in Section 3.2.

3.4.3. *Bifunctional GDE with optimal Ni/NiO content*

Sample B2 contained 23 wt% Ni and was aged under repeated OER/ORR cycling in the absence of zincates. In the previous analysis at the Mn L-edge [1], this sample displayed a more homogeneous Mn distribution compared to B1, with larger areas maintaining balanced Mn (III)/Mn(IV) ratios. Localized regions of Mn(II) formation were still observed, but to a lesser extent, reflecting improved redox reversibility due to the higher Ni content. The Ni(0)/Ni(II) ratio map reconstructed from ptychography is shown in Fig. 7c, together with the Mn chemical-state maps in Fig. 7b. The Ni distribution appears more uniform than in B1, with oxidation states varying within narrower ranges. Domains with favorable Mn(III)/Mn(IV) ratios correlate with areas of moderate Ni oxidation, suggesting cooperative stabilization between the two elements. Hotspots of Mn(II) accumulation remain visible, but these coincide with zones of highly oxidized Ni (low Ni(0)/Ni(II) ratios), pointing to localized electrochemical overload or compositional inhomogeneity. Overall, the correlation of Ni and Mn maps in B2 confirms that increased Ni content enhances the resilience of the catalyst against degradation. Ni not only contributes to improved electronic conductivity but also appears to buffer Mn redox fluctuations, leading to more extended regions of active and reversible Mn chemistry compared with B1. The improved electrochemical stability inferred from the Ni–Mn maps reflects what is discussed in Section 3.2.

3.4.4. *Bifunctional GDE with optimal Ni/NiO content, cycled in presence of zincates*

Sample B3 contained 23 wt% Ni and was aged under repeated OER/ORR cycling in the presence of zincates. In the Mn analysis reported in [1], this sample exhibited a higher degree of degradation compared to B2 despite having the same Ni content. Specifically, Mn maps revealed extensive formation of Mn(II) together with evidence of dissolution and redeposition processes promoted by zincates. These features indicated that the protective effect of Ni was less effective under these cycling conditions. The Ni(0)/Ni(II) ratio map reconstructed from ptychography is shown in Fig. 8c, together with the Mn maps from [1] in Fig. 8b. Compared to B2, the Ni distribution in B3 is less uniform, with broader variations in oxidation state. Regions where Mn reduction was most pronounced also displayed higher Ni oxidation, suggesting that under zincate-rich conditions both elements undergo destabilization. The average Ni(0)/Ni(II) ratio reported for this sample (Table 1) is consistent with localized reduction of Ni, further supporting the observation that zincates promote redox imbalance across the electrode. A noteworthy observation is that Ni also appears in regions where Mn(II) accumulation is most pronounced. This spatial co-localization is directly evidenced by the correlative maps, whereas its mechanistic origin cannot be established from the present measurements. Possible interpretations include zincate-promoted Mn dissolution and reprecipitation, with Ni locally interacting with the redeposited *Mn species*, or transient Ni redox responses to the altered local chemical environment. More generally, the spatial organization of the chemical states observed in these maps can be interpreted within the morphochemical framework of the DIB model, as discussed in Section 3.4.1 and demonstrated through representative fitting of the Mn chemical-state maps in the Supporting Information.

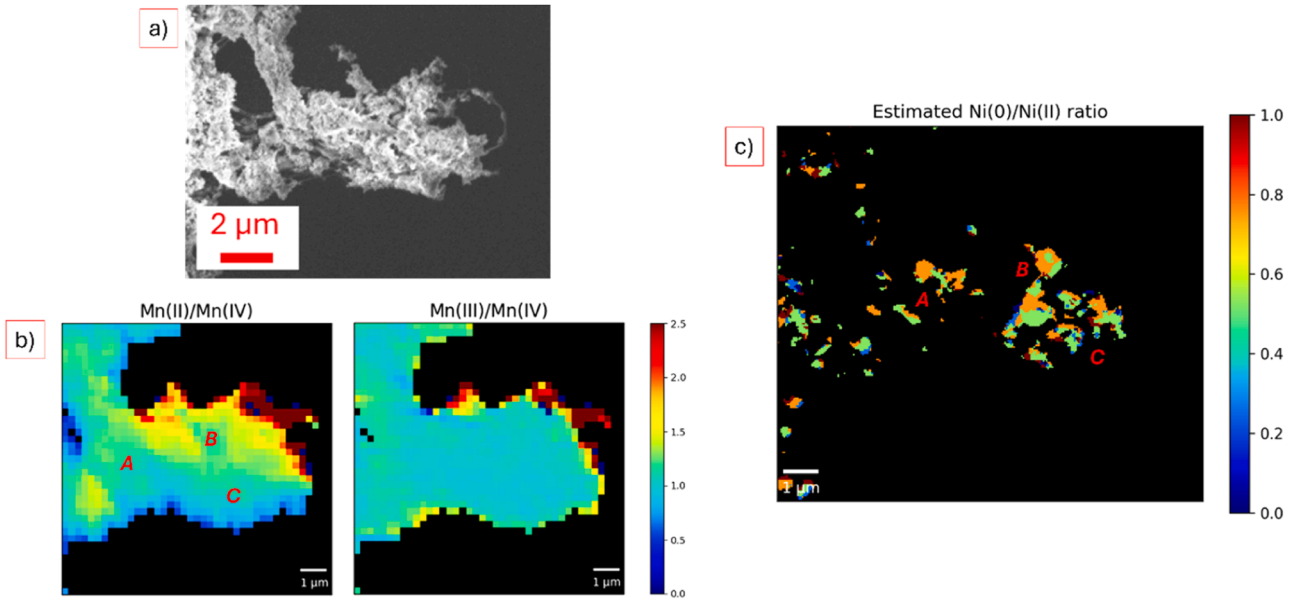


Fig. 7. Analyses on sample B2 (a) SEM image of the cluster under analysis. (b) Chemical ratio maps: Mn(II)/Mn(IV) (left) and Mn(III)/Mn(IV) (right). (c) Ni(0)/Ni(II) distribution map. Letters A, B, and C indicate matched points across all panels.

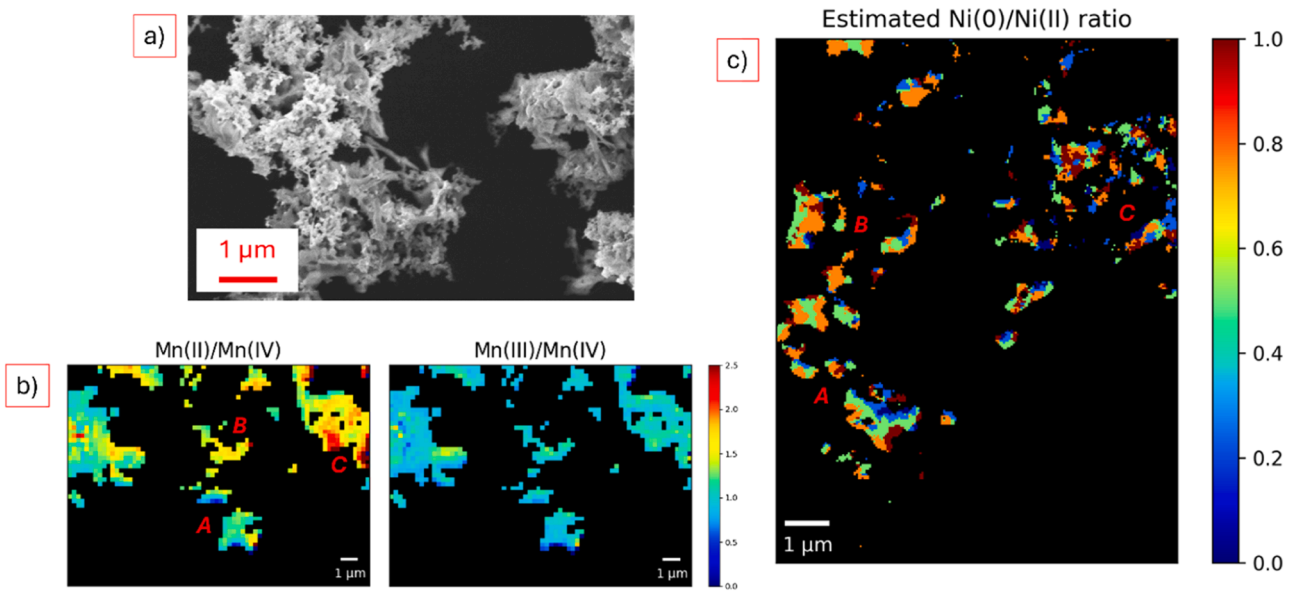


Fig. 8. Analyses on sample B3 (a) SEM image of the cluster under analysis. (b) Chemical ratio maps: Mn(II)/Mn(IV) (left) and Mn(III)/Mn(IV) (right). (c) Ni(0)/Ni(II) distribution map. Letters A, B, and C indicate matched points across all panels.

These scenarios should therefore be regarded as working hypotheses rather than demonstrated mechanisms. Their discrimination would require dedicated, preferably operando, experiments and lies beyond the scope of the present study. These spectromicroscopy observations are in agreement with the electrochemical behavior discussed in Section 3.2.

4. Conclusions

In this work, we extended our previous STXM study of Mn-based gas diffusion electrodes [1] by applying soft X-ray ptychography at the Ni L-edge to the same samples and TEM grids. The adoption of KK-based reconstruction enabled the retrieval of chemically meaningful absorption-equivalent spectra from phase data, thereby overcoming the intrinsic limitations of absorption contrast in detecting weak or nanometrically dispersed species. The validation steps confirmed that the workflow reliably distinguishes pixels containing usable spectra, reproduces absorption features from phase data, and reconstructs complete spectral stacks that preserve chemical interpretability across the field of view.

Application of this approach to three bifunctional electrodes revealed how Ni and Mn interact under electrochemical cycling. In B1, with low Ni content, Ni appeared in localized oxidized domains that overlapped with regions of irreversible Mn reduction, confirming the limited stabilizing capacity of Ni at insufficient loading. In B2, with optimized Ni content, Ni was more uniformly distributed and correlated with zones where Mn maintained reversible redox activity, demonstrating a cooperative stabilization effect. In B3, cycled in the presence of zincates, this stabilizing role was compromised: Mn maps showed extensive reduction and dissolution, and Ni exhibited heterogeneous distributions with partial reduction. A noteworthy observation was the co-localization of Ni with Mn(II)-rich regions, which is consistent with zincates promoting complex processes such as Mn dissolution and reprecipitation, potentially buffered locally by Ni.

These results show that soft X-ray ptychography, coupled with KK-based spectral reconstruction, provides access to chemical information that is otherwise inaccessible by absorption-based STXM alone. Beyond validating the methodology, the present study offers new insights into the nanoscale interplay between Ni and Mn in bifunctional catalysts and highlights the importance of operando-compatible spectromicroscopy for unraveling degradation mechanisms in Zn–air batteries. Finally, the combined GCD and EIS analyses integrate smoothly with their spectromicroscopic counterpart. The largest increase in polarization resistance was observed for B1, where Mn(II) accumulation was most pronounced, whereas B2 showed the most limited R_{pol} variation, consistent with its more homogeneous Ni distribution and more balanced Mn redox chemistry. B3 showed an intermediate impedance evolution, in agreement with a more complex zincate-mediated degradation pathway, implying the coexistence of multiple degradation mechanisms. The consistency between the nanoscale spectromicroscopy observations and the independently derived impedance trends further supports the proposed interpretation of Ni-assisted stabilization and zincate-mediated degradation pathways.

CRediT authorship contribution statement

Alessandro Alleva: Writing – original draft, Visualization, Validation, Software, Methodology, Investigation, Formal analysis, Data curation, Conceptualization. **Francesco Guzzi:** Writing – review & editing, Visualization, Validation, Software, Methodology, Investigation, Formal analysis, Data curation. **Massimo Frittelli:** Conceptualization, Data curation, Formal analysis, Investigation, Methodology, Software, Validation, Visualization, Writing – review & editing. **George Kourousias:** Writing – review & editing, Validation, Software, Methodology, Formal analysis, Data curation, Conceptualization. **Valentina Bonanni:** Writing – review & editing, Investigation, Formal analysis. **Alessandra Gianoncelli:** Writing – review & editing, Validation, Methodology, Investigation, Formal analysis, Data curation, Conceptualization. **Ivonne Sgura:** Conceptualization, Data curation, Formal analysis, Investigation, Methodology, Software, Validation, Visualization, Writing – review & editing. **Milan Žižić:** Writing – review & editing, Investigation, Formal analysis. **Benedetto Bozzini:** Writing – review & editing, Visualization, Validation, Supervision, Resources, Project administration, Methodology, Investigation, Funding acquisition, Formal analysis, Data curation, Conceptualization.

Declaration of competing interest

The authors declare that they have no known competing financial interests or personal relationships that could have appeared to influence the work reported in this paper.

Acknowledgements

This research is part of the PhD project "Fabrication of gas diffusion electrodes for zinc air batteries and multi-method study of their degradation pathways" supported by CERIC-ERIC. We acknowledge Elettra Sincrotrone Trieste for providing access to its synchrotron radiation facilities and for financial support under the SUI internal project.

Co-funding was received from ZnOrgBat project (no. 23034) under the EIT RawMaterials, part of the Horizon Europe funding scheme.

Supplementary materials

Supplementary material associated with this article can be found, in the online version, at doi:10.1016/j.electacta.2026.149982.

Data availability

Data will be made available on request.

References

[1] B. Bozzini, A. Alleva, V. Bonanni, R. Ciancio, G. Kourousias, F. Guzzi, A. Gianoncelli, Degradation of α-MnO2 in Zn-air battery gas-diffusion electrodes: an investigation based on chemical-state mapping, Electrochim. Acta 513 (2025) 145534.
[2] V. Caramia, B. Bozzini, Materials science aspects of zinc–air batteries: a review, Mater. Renew. Sustain. Energy 3 (2) (2014) 28.
[3] S. Ren, X. Duan, S. Liang, M. Zhang, H. Zheng, Bifunctional electrocatalysts for Zn–air batteries: recent developments and future perspectives, J. Mater. Chem. A 8 (13) (2020) 6144–6182.
[4] H.F. Wang, C. Tang, Q. Zhang, A review of precious-metal-free bifunctional oxygen electrocatalysts: rational design and applications in Zn– air batteries, Adv. Funct. Mater. 28 (46) (2018) 1803329.
[5] X.W. Lv, Z. Wang, Z. Lai, Y. Liu, T. Ma, J. Geng, Z.Y. Yuan, Rechargeable zinc–air batteries: advances, challenges, and prospects, Small 20 (4) (2024) 2306396.
[6] Y. Kumar, M. Mooste, K. Tammeveski, Recent progress of transition metal-based bifunctional electrocatalysts for rechargeable zinc–air battery application, Curr. Opin. Electrochem. 38 (2023) 101229.
[7] A.R. Mainar, L.C. Colmenares, O. Leonet, F. Alcaide, J.J. Iruin, S. Weinberger, J. A. Blazquez, Manganese oxide catalysts for secondary zinc air batteries: from electrocatalytic activity to bifunctional air electrode performance, Electrochim. Acta 217 (2016) 80–91.
[8] A.S. Ryabova, F.S. Napolskiy, T. Poux, S.Y. Istomin, A. Bonnefont, D.M. Antipin, E. R. Savinova, Rationalizing the influence of the Mn (IV)/Mn (III) red-ox transition on the electrocatalytic activity of manganese oxides in the oxygen reduction reaction, Electrochim. Acta. 187 (2016) 161–172.
[9] O. Diaz-Morales, D. Ferrus-Suspedra, M.T. Koper, The importance of nickel oxyhydroxide deprotonation on its activity towards electrochemical water oxidation, Chem. Sci. 7 (4) (2016) 2639–2645.
[10] V. Vij, S. Sultan, A.M. Harzandi, A. Meena, J.N. Tiwari, W.G. Lee, K.S. Kim, Nickel-based electrocatalysts for energy-related applications: oxygen reduction, oxygen evolution, and hydrogen evolution reactions, ACS. Catal. 7 (10) (2017) 7196–7225.
[11] Y.L. Cao, H.X. Yang, X.P. Ai, L.F. Xiao, The mechanism of oxygen reduction on MnO2-catalyzed air cathode in alkaline solution, J. Electroanal. Chem. 557 (2003) 127–134.
[12] E. Marini, L. Jörissen, S. Brimaud, Rational design of a low-cost, durable and efficient bifunctional oxygen electrode for rechargeable metal-air batteries, J. Power. Sources. 482 (2021) 228900.
[13] Y. Salman, S. Waseem, A. Alleva, P. Banerjee, V. Bonanni, E. Emanuele, B. Bozzini, Synthesis, characterization, functional testing and ageing analysis of bifunctional Zn-air battery GDEs, based on α-MnO2 nanowires and Ni/NiO nanoparticle electrocatalysts, Electrochim. Acta 469 (2023) 143246.
[14] B. Bozzini, A. Goldoni, Will in situ synchrotron-based approaches beat the durability issues of next-generation batteries? J. Phys. D. Appl. Phys. 51 (5) (2018) 050201.
[15] K.T. Arul, H.W. Chang, H.W. Shiu, C.L. Dong, W.F. Pong, A review of energy materials studied by in situ/operando synchrotron x-ray spectro-microscopy, J. Phys. D. Appl. Phys. 54 (34) (2021) 343001.
[16] E. Emanuele, A.G. Agrios, A. Alleva, V. Bonanni, R. Ciancio, A. Gianoncelli, B. Bozzini, Carbon-cloth supported ZnO nanorods as binder-free zinc-ion battery anodes: an investigation into the electrode formation process, Adv. Sustain. Syst. 9 (2025) 2400921.
[17] H. Zhao, H.D. Deng, A.E. Cohen, J. Lim, Y. Li, D. Fraggedakis, M.Z. Bazant, Learning heterogeneous reaction kinetics from X-ray videos pixel by pixel, Nature 621 (7978) (2023) 289–294.
[18] P. Thibault, M. Dierolf, C.M. Kewish, A. Menzel, O. Bunk, F. Pfeiffer, Contrast mechanisms in scanning transmission x-ray microscopy, Phys. Rev. A—Atomic, Molecular, and Optical Physics 80 (4) (2009) 043813.
[19] P.D. Quinn, F. Cacho-Nerin, M.A. Gomez-Gonzalez, J.E. Parker, T. Poon, J. M. Walker, Differential phase contrast for quantitative imaging and spectro-microscopy at a nanoprobe beamline, Synchrotron Radiat. 30 (1) (2023) 200–207.
[20] F. Pfeiffer, X-ray ptychography, Nat. Photonics. 12 (1) (2018) 9–17.
[21] A.M. Wise, J.N. Weker, S. Kalirai, M. Farmand, D.A. Shapiro, F. Meirer, B. M. Weckhuysen, Nanoscale chemical imaging of an individual catalyst particle with soft X-ray ptychography, ACS. Catal. 6 (4) (2016) 2178–2181.
[22] D.A. Shapiro, Y.S. Yu, T. Tyliszczak, J. Cabana, R. Celestre, W. Chao, H. A. Padmore, Chemical composition mapping with nanometre resolution by soft X-ray microscopy, Nat. Photonics. 8 (10) (2014) 765–769.
[23] B. Mook Weon, J. Ho Je, Y. Hwu, G. Margaritondo, Phase contrast x-ray imaging, Int. J. Nanotechnol. 3 (2–3) (2006) 280–297.
[24] C. Raven, A. Snigirev, I. Snigireva, P. Spanne, A. Souvorov, V. Kohn, Phase-contrast microtomography with coherent high-energy synchrotron x rays, Appl. Phys. Lett. 69 (13) (1996) 1826–1828.
[25] G. Kourousias, B. Bozzini, M.W. Jones, G.A. Van Riessen, S. Dal Zilio, F. Billè, A. Gianoncelli, Monitoring dynamic electrochemical processes with in situ ptychography, Appl. Nanosci. 8 (4) (2018) 627–636.
[26] B. Watts, Calculation of the Kramers-Kronig transform of X-ray spectra by a piecewise Laurent polynomial method, Opt. Express. 22 (19) (2014) 23628.
[27] B. Bozzini, G. Kourousias, A. Gianoncelli, M.W. Jones, G. Van Riessen, M. Kiskinova, Soft X-ray ptychography as a tool for in operando morphochemical studies of electrodeposition processes with nanometric lateral resolution, J. Electron. Spectros. Relat. Phenomena 220 (2017) 147–155.
[28] A. Gianoncelli, G. Kourousias, L. Merolle, M. Altissimo, A. Bianco, Current status of the TwinMic beamline at Elettra: a soft X-ray transmission and emission microscopy station, Synchrotron Radiat. 23 (6) (2016) 1526–1537.
[29] A. Gianoncelli, V. Bonanni, G. Gariani, F. Guzzi, L. Pascolo, R. Borghes, G. Kourousias, Soft X-ray microscopy techniques for medical and biological imaging at TwinMic—Elettra, Appl. Sci. 11 (16) (2021) 7216.
[30] F. Guzzi, G. Kourousias, F. Billè, R. Pugliese, A. Gianoncelli, S. Carrato, A modular software framework for the design and implementation of ptychography algorithms, PeerJ. Comput. Sci. 8 (2022) e1036.
[31] A. Maiden, D. Johnson, P. Li, Further improvements to the ptychographical iterative engine, Optica 4 (7) (2017) 736.
[32] P. Thibault, A. Menzel, Reconstructing state mixtures from diffraction measurements, Nature 494 (7435) (2013) 68–71.
[33] M.A. Marcus, Data analysis in spectroscopic STXM, J. Electron. Spectros. Relat. Phenomena 264 (2023) 147310.
[34] B. Bozzini, D. Lacitignola, I. Sgura, Spatio-temporal organization in alloy electrodeposition: a morphochemical mathematical model and its experimental validation, J. Solid. State Electrochem. 17 (2) (2013) 467–479.
[35] D. Lacitignola, B. Bozzini, I. Sgura, Spatio-temporal organization in a morphochemical electrodeposition model: hopf and Turing instabilities and their interplay, Eur. J. Appl. Math. 26 (2) (2015) 143–173.
[36] M. Kazemian, F. Rossi, A. Casaroli, T. Caielli, B. Kaulich, M. Kiskinova, B. Bozzini, X-ray imaging and micro-spectroscopy unravel the role of zincate and zinc oxide in the cycling of zinc anodes in mildly acidic aqueous electrolytes, J. Power. Sources. 524 (2022) 231063.
[37] I. Sgura, L. Mainetti, F. Negro, M.G. Quarta, B. Bozzini, Deep-learning based parameter identification enables rationalization of battery material evolution in complex electrochemical systems, J. Comput. Sci. 66 (2023) 101900.